Rapid Communications

Electronic structure of full-shell InAs/Al hybrid semiconductor-superconductor nanowires: Spin-orbit coupling and topological phase space

Benjamin D. Woods,[1] Sankar Das Sarma,[2] and Tudor D. Stanescu[1,2]

[1]*Department of Physics and Astronomy, West Virginia University, Morgantown, West Virginia 26506, USA*

[2]*Condensed Matter Theory Center and Joint Quantum Institute, Department of Physics, University of Maryland, College Park, Maryland 20742-4111, USA*

(Received 4 February 2019; revised manuscript received 2 April 2019; published 26 April 2019)

We study the electronic structure of full-shell superconductor-semiconductor nanowires, which have recently been proposed for creating Majorana zero modes, using an eight-band $\vec{k}\cdot\vec{p}$ model within a fully self-consistent Schrödinger-Poisson scheme. We find that the spin-orbit coupling induced by the intrinsic radial electric field is generically weak for subbands with their minimum near the Fermi energy. Furthermore, we show that the chemical potential windows consistent with the emergence of a topological phase are small and sparse and can only be reached by fine-tuning the diameter of the wire. These findings suggest that the parameter space consistent with the realization of a topological phase in full-shell InAs/Al nanowires is, at best, very narrow.

DOI: 10.1103/PhysRevB.99.161118

Hybrid semiconductor-superconductor (SM-SC) nanowires have recently become the subject of intense research in the context of the quest for topological Majorana zero modes (MZMs) [1,2]. Motivated by the promise of fault-tolerant topological quantum computation [3,4] and following concrete theoretical proposals [5–7], this nanowire-based MZM search has shown impressive experimental progress in the past few years [8–17]. Nonetheless, reaching the level of the definitive demonstration and consistent realization of isolated MZMs requires further development and improvement. The lack of definitive evidence of topological Majorana behavior, e.g., correlated tunneling features at the opposite ends of the system [18], and the real possibility of having trivial low-energy Andreev bound states (ABSs) mimicking the MZM phenomenology [19–24], instead of actual MZMs, underscore the importance of being able to finely control the electrochemical potential in gated devices and to engineer structures with large effective g factors and spin-orbit couplings, which represent key necessary conditions for creating/stabilizing nanowire-based MZMs.

To alleviate some of these rather stringent requirements and the associated problems, an alternative path to creating MZMs, which uses magnetic flux applied to SM wires coated with a full SC shell, was recently proposed [25,26]. This scheme eliminates the need for a large Zeeman splitting (i.e., large effective g factor or large magnetic field) and also generates a more uniform and reproducible electrostatic environment (which may help avoid creating trivial ABSs). The main disadvantages of this approach are the impossibility of directly controlling the chemical potential using gates and absence of a large electric field across the wire to ensure strong spin-orbit coupling. While the chemical potential can be tuned by controlling the diameter of the wire (i.e., using different samples), a spin-orbit coupling strength on the order of 200 meV Å (or larger) is required to access the topological phase [26]. Since these parameters cannot be directly measured experimentally, obtaining reliable theoretical estimates represents an essential task. To capture the basic physics, it is critical to take into account (i) the multiorbital nature of the SM bands (by incorporating at least s- and p-orbital contributions) and (ii) the electrostatic effects (by self-consistently solving a Schrödinger-Poisson problem). We note that these are crucial issues for the entire research field of SM-SC hybrid nanostructures, but they have only recently started to be addressed, and only within single-orbital approaches [27–31].

In this work, we determine the spin-orbit coupling, chemical potential, and effective mass for full-shell InAs/Al nanowires based on an eight-band $\vec{k}\cdot\vec{p}$ model [32] using a mean-field treatment of the long-range electron-electron interaction within a fully self-consistent Schrödinger-Poisson scheme. We find that the chemical potential windows consistent with the emergence of a topological phase form a sparse set and require extreme fine-tuning of the wire diameter. Furthermore, we find that the spin-orbit coupling is weak (on the order of 30–60 meV Å) for all physically relevant values of the wire diameter and SM-SC work function difference, making any emergent topological superconducting phase very weakly protected by a small gap. Based on these findings, we conclude that realizing topological superconductivity and MZMs in full-shell SM-SC nanowires represents a low-success-probability target. If realized, the topological phase is likely to be characterized by a small topological gap. We also provide suggestions for possible optimizations of the full-shell scheme.

We consider a cylindrical full-shell nanowire, as represented schematically in Fig. 1(a). The SM core is modeled using an eight-band $\vec{k}\cdot\vec{p}$ model [32–34] in the presence of a mean-field effective potential,

$$H = H_{\vec{k}\cdot\vec{p}} - e\phi(r), \tag{1}$$

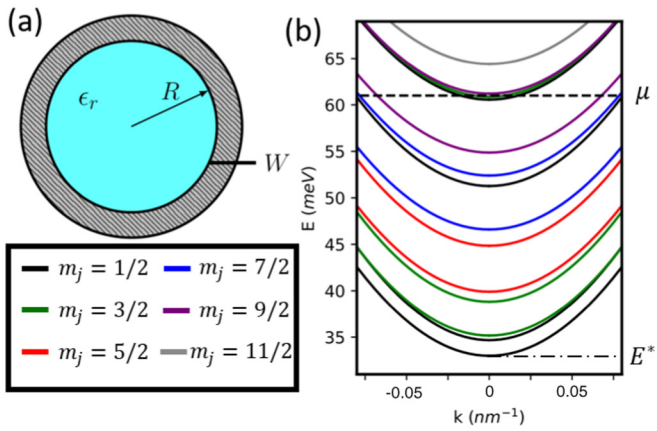

FIG. 1. (a) Cross section of a full-shell nanowire consisting of an InAs core (blue) and an Al shell (gray). The SC-SM interface (characterized by the work function difference W) is treated as a Dirichlet boundary condition. (b) Low-energy conduction-band structure obtained by solving Eqs. (1) and (2) self-consistently. The colors designate pairs of bands corresponding to given m_J quantum numbers (labeling the z component of total angular momentum). The chemical potential μ and zero-point energy E^* are marked by the dashed and dashed-dotted lines, respectively.

where the mean-field potential $\phi(r)$ is induced by the net charge inside the SM wire and must be determined self-consistently. While other approaches, such as density functional theory and empirical tight-binding methods [35,36], are known to accurately capture the electronic structure of semiconductors, $\vec{k}\cdot\vec{p}$ methods are much less computationally demanding and are quite accurate near the high-symmetry points of the Brillouin zone, which are of interest here [37]. Note that InAs nanowires grown along the [111] crystallographic direction have a hexagonal cross section, but the cylindrical approximation used here for simplicity is expected to be quite accurate [38]. In addition, we adopt the so-called axial approximation, which amounts to promoting the underlying atomic fcc lattice symmetry to a full rotation symmetry abut the z axis [32], so that the z component of the angular momentum, J_z, is conserved (see the Supplemental Material for details [39]).

The mean-field potential $\phi(r)$ is determined by solving the Poisson equation

$$\nabla^2\phi(r) = -\frac{\rho(r)}{\epsilon}, \tag{2}$$

where ρ is the charge density corresponding to the occupied conduction-band states and $\epsilon = \epsilon_r\epsilon_o$, with $\epsilon_r = 15$, is the lattice dielectric constant of InAs. The chemical potential is determined by the work function difference between the SM and the SC (W) and by the energy of conduction-band edge (E_o for bulk InAs). In the full-shell geometry, W and E_o are not independent parameters (as they are in a "standard" gated configuration, where the chemical potential μ is tuned independently) and they can be combined as

$$\mu = W - E_o. \tag{3}$$

With this definition of the chemical potential, the boundary condition at the SM-SC interface [28–30] becomes $\phi(R) = 0$, as the global band shift due to the work function difference is already incorporated in μ. Finally, we note that the SC shell is not explicitly included in our model, but serves as an electrostatic boundary condition (through the work function difference W). While the presence of a SC is known to renormalize the band structure of the hybrid system [21,28–30,45–47], the goal of this work is to determine the "bare," i.e., unrenormalized wire parameters characterizing the self-consistent electronic structure of the full-shell system.

The Schrödinger equation, $H\Psi = E\Psi$, where Ψ is an eight-component spinor, and the Poisson equation (2) are solved self-consistently. For the cylindrical geometry and within the axial approximation, we have

$$\Psi_{m_J}(\vec{r}, k_z) = \frac{g_{m_J}(r, k_z)}{\sqrt{r}} e^{ik_z z} e^{i(m_J - M_s)\varphi}, \tag{4}$$

where $g_{m_J}(r, k_z)$ is an eight-component spinor, $m_J \in (\mathbb{Z} + \frac{1}{2})$ labels the z component of the total angular momentum, and $M_s = \mathrm{diag}(\frac{1}{2}, -\frac{1}{2}, \frac{3}{2}, \frac{1}{2}, -\frac{1}{2}, -\frac{3}{2}, \frac{1}{2}, -\frac{1}{2})$ is a diagonal matrix. The first two entries represent s orbitals, the next four are p orbitals with angular momentum $j = 3/2$, and the last two are p orbitals with $j = 1/2$.

The band structure for a prototypical full-shell wire of radius $R = 45$ nm with $\mu = 62$ meV is shown in Fig. 1(b). Only the conduction subbands are shown. At zero magnetic field, the states corresponding to m_J and $-m_J$ have the same energy, hence all subbands are double degenerate. Note that each m_J value corresponds to two subbands separated by a finite energy gap. The subbands consist of nearly opposite spin states with dominant orbital angular momentum ℓ and $\ell + 1$. All states up to the chemical potential μ (dashed line in Fig. 1) are filled. The energy E^* corresponding to the bottom of the conduction band is the zero-point energy due to finite size confinement and the mean-field effective potential $\phi(r)$.

The emergence of a topological SC phase supporting MZMs in cylindrical full-shell nanowires requires a finite magnetic field inducing a phase winding in the superconducting order parameter and a chemical potential lying near the bottom of an $m_J = \frac{1}{2}$ subband [26]. To determine the likelihood of the chemical potential satisfying this condition, we calculate the band structure of a nanowire of radius $R = 45$ nm as a function of μ, i.e., the work-function difference W. The (total) number of occupied $m_J \geqslant \frac{1}{2}$ subbands, as well as the number of $m_J = \frac{1}{2}$ subbands, are shown in Fig. 2(a). While W and E_o (hence μ) are not precisely known, one would expect a chemical potential on the order $\sim 10^2$ meV. As shown in Fig. 2(a), this corresponds to a large number of occupied subbands (tens of bands). In addition, the system has a few occupied $m_J = \frac{1}{2}$ subbands (red dashed line). The values of μ consistent with the chemical potential being within ± 0.5 meV of the bottom of an $m_J = \frac{1}{2}$ subband (i.e., within an energy window about four times the induced gap) are marked by the green shadings. These regions correspond to (rather optimistic estimates of) parameter values consistent with the emergence of MZMs [26]. Note that the width

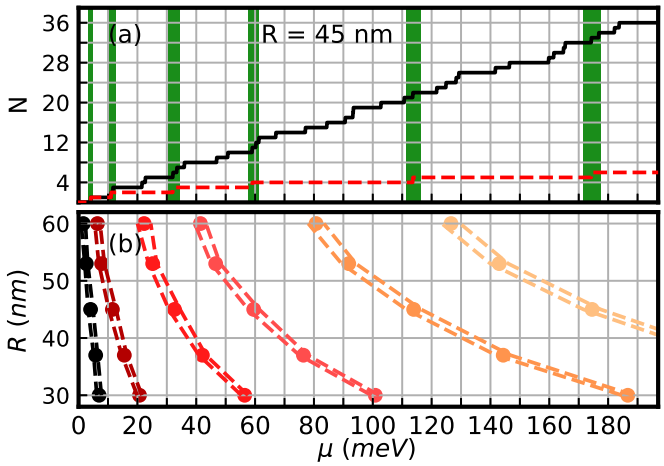

FIG. 2. (a) Number of occupied $m_J \geqslant \frac{1}{2}$ and $m_J = \frac{1}{2}$ subbands as a function of μ are shown in black (solid) and red (dashed) lines, respectively, for a wire of radius $R = 45$ nm. Green shaded regions show when the bottom of an $m_J = \frac{1}{2}$ subband is within 0.5 meV of the chemical potential. (b) Dashed lines show boundaries of when $m_J = \frac{1}{2}$ subband is within 0.5 meV of the chemical potential as a function of μ and R. Note that for any μ there is a subband crossing for a suitable radius R.

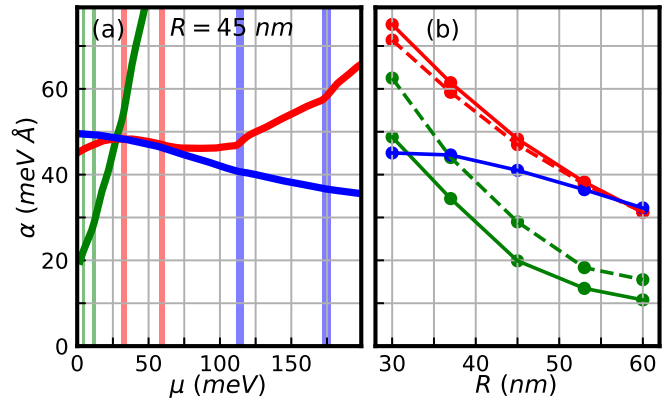

FIG. 3. (a) Spin-orbit coupling coefficient α as a function of μ for the first three $m_J = \frac{1}{2}$ subband pairs (green, red, and blue lines, respectively) in a wire with $R = 45$ nm. The subband bottoms lie within ± 0.5 meV of the chemical potential within the corresponding shaded regions [see also Fig. 2(a)]. (b) Spin-orbit coupling coefficient α for the $m_J = \frac{1}{2}$ subband pair at chemical potential crossings as a function of R. The colors correspond to those in panel (a) with the solid and dashed lines denoting the first and second crossing of a subband pair, respectively.

of these regions increases with μ, because the mean-field potential increases and it becomes more "expensive" to add charge to the system. At the same time, however, the "green regions" become more sparse. Basically, Fig. 2(a) demonstrates that, for a full-shell wire of radius $R = 45$ nm, the likelihood of satisfying conditions (i.e., having W and E_o values) consistent with the emergence of MZMs is rather low. To establish the dependence of this likelihood on the wire radius, we perform self-consistent band-structure calculations for different values of R and identify the regions of "suitable" chemical potential. The results are shown in Fig. 2(b). Note that the intervals between the "suitable" regions decrease with increasing radius. Also, since μ should be independent of R (as is determined by the SC-SM work-function difference W), Fig. 2(b) shows that the system can be brought into a regime consistent with the emergence of MZMs by (finely) tuning the radius of the wire within the 30–60 nm range. Note, however, that the fine-tuning requirement becomes more stringent at large values of the chemical potential. This also implies that, if a wire of radius R supports a topological SC phase, wires with slightly different radii, e.g., $R \pm 5$ nm, should *not* be able to support topological phases. Finally, we emphasize that these considerations hold under the assumption that the value of the work-function difference, W, is relatively stable from device to device (otherwise, the realization of the topological condition becomes purely a matter of chance and wild luck).

Next, we investigate the spin-orbit coupling and extract effective parameters for the two-band model Hamiltonian H_{eff} recently used to study the topological properties of full-shell nanowires [26]. Explicitly, we have

$$H_{\text{eff}} = \frac{\hbar^2 k^2}{2m^*} - \mu + \alpha \hat{r} \cdot [\vec{\sigma} \times \vec{k}], \tag{5}$$

where m^* is the effective mass, μ is the chemical potential, σ_i $(i = x, y, z)$ are the Pauli spin matrices, and α is a phenomenological spin-orbit coupling coefficient. Again, since the system has cylindrical symmetry, $m_J \in (\mathbb{Z} + \frac{1}{2})$ is a good quantum number and each m_J value labels a pair of subbands separated by a k_z-dependent energy gap. We determine the spin-orbit coupling α and the effective mass m^* by fitting a given pair of subbands of the full eight-band model with the corresponding m_J pair of the effective Hamiltonian (5). The details of the extraction procedure are provided in the Supplemental Material [39].

The effective spin-orbit coupling coefficients corresponding to the $m_J = \frac{1}{2}$ states for a wire of radius $R = 45$ nm are shown in Fig. 3. Only the first three pairs are represented, as the higher energy pairs occur for $\mu > 200$ meV, but we checked that the main features hold for larger values of the chemical potential. The spin-orbit coefficient associated with the first $m_J = \frac{1}{2}$ pair (shown in green) increases nearly linearly with μ, i.e., with the work-function difference W [see panel (a)]. However, this pair is relevant for topological physics only in the regime $\mu < 10$ meV, when it is close enough to the chemical potential (shaded green ranges). Similarly, the relevant values of α associated with the higher energy pairs are those within the corresponding "topological" windows, as determined in Fig. 2(a). For example, if $\mu \approx 175$ meV, the only relevant contribution to a possible topological phase is given by the second component of the third $m_J = \frac{1}{2}$ pair, which is characterized by $\alpha \approx 37$ meV Å. Although the second pair has $\alpha \approx 58$ meV Å and the first pair has an even larger spin-orbit coupling, they are very far from the chemical potential and cannot induce a topological quantum phase transition.

The main result shown in Fig. 3(a) is that the effective spin-orbit coupling of $m_J = \frac{1}{2}$ subbands located in the vicinity of the chemical potential does not exceed 50 meV Å in a wire of radius $R = 45$ nm, *regardless of the work-function*

difference. To determine the dependence of the spin-orbit coupling strength on the radius of the wire, we calculate the effective coupling of $m_J = \frac{1}{2}$ subbands that lie in the vicinity of the chemical potential for wires with $30 \leqslant R \leqslant 60$ nm. The results are shown in Fig. 3(b). First, we note that for a given $m_J = \frac{1}{2}$ pair the spin-orbit coupling (at the chemical potential) decreases with increasing wire radius. Qualitatively, this can be understood as follows: increasing R reduces the interband spacings, so that the chemical potential crossing (for a given subband) will occur at a lower value of μ, i.e., in the presence of less charge inside the wire, hence a weaker mean-field potential. In turn, the reduced potential generates a weaker spin-orbit coupling. The second property revealed by the results shown in panel (b) is that the overall magnitude of the spin-orbit coupling for $m_J = \frac{1}{2}$ subbands in the vicinity of the chemical potential remains small (i.e., $\alpha < 75$ meV Å) *regardless of radius*, i.e., for wires with $30 \leqslant R \leqslant 60$ nm and arbitrary work function (so that $0 < \mu < 200$ meV). We remind the reader that the predicted spin-orbit coupling strength required for the realization of topological superconductivity is on the order of 200 meV Å (or larger) [26]. The central result of this work, shown in Fig. 3, demonstrates that such values of the effective spin-orbit coupling cannot be realized in full-shell InAs nanowires. Note that reducing the radius of the wire may increase the effective spin-orbit coupling, but finding a radius that is consistent with the emergence of topological superconductivity may become a challenging task, as discussed in the context of Fig. 2(b). The whole procedure then becomes a matter of time-consuming trial and error dependent on getting "lucky."

To better understand the physical reason behind the small spin-orbit coupling values at the chemical potential, we calculate the wave functions of the first six $m_J = \frac{1}{2}$ states at $k_z = 0$ for a wire of radius $R = 45$ nm with $\mu = 57$ meV. The results are shown in Fig. 4. Note that the wave-function amplitudes are shifted with respect to the bottom of the mean-field potential (gray shading) by the energies of the corresponding states, allowing us to visualize the effect of $\phi(r)$ on various states. The first two states ($p = 1$) are localized near the surface of the SM wire (i.e., the SM-SC interface). This is not surprising, as their energy is below the top of the mean-field potential, which effectively pushes them away from the center of the wire. Since the electric field $\boldsymbol{E} = -\nabla\phi$ is maximum in the outer region $30 \leqslant r \leqslant 45$ nm, one would expect a relatively strong spin-orbit coupling for this pair of states ($\alpha > 80$ meVÅ; see Fig. 3). By contrast, the second and third pairs of states have energies well above the potential maximum and are weakly affected by $\phi(r)$. As a result, these states are extended throughout the entire cross section of the wire and the effect of the radial electric field will be strongly suppressed, resulting in lower values of the spin-orbit coupling ($\alpha \approx 47$ meV Å in Fig. 3). In conclusion, we studied the electronic structure of full-shell InAs/Al hybrid nanowires using an eight-band $\vec{k} \cdot \vec{p}$ model which was solved within a fully self-consistent Schrödinger-Poisson scheme. We found that the spin-orbit coupling of the $m_J = \pm\frac{1}{2}$ subbands near the chemical potential is generically small $\alpha < 70$ meV Å, regardless of the chemical potential (i.e., the work-function difference between the SM wire and the SC shell) or the wire diameter. In addition, we demonstrated that bringing the bottom of an $m_J = \pm\frac{1}{2}$ subband close to the chemical potential requires fine-tuning the wire radius. More specifically, within the range $30 \leqslant R \leqslant 60$ nm one should expect to find about two small windows (each a few nanometers wide) consistent with the presence of an $m_J = \pm\frac{1}{2}$ subband near the chemical potential. Since the existence of low-energy $m_J = \pm\frac{1}{2}$ subbands with strong effective spin-orbit coupling is critical for the emergence of a topological phase in full-shell nanowires, our findings suggest that the parameter space consistent with such a phase may be, at best, very narrow. As a possible solution for enhancing the spin-orbit coupling, we suggest using core-shell SM wires, with a wide gap material (e.g., GaAs) for the core and a narrow-gap SM (e.g., InAs) for the shell. In essence, the presence of the core will push the states toward the outer region, where the radial electric field is large, increasing the spin-orbit coupling. Another possibility is to grow InAs in a wurzite phase, which is known to have larger spin-orbit coupling [48,49]. Finally, we note that the presence of symmetry-breaking perturbations (e.g., due to the hexagonal wire geometry) is unlikely to generate a dramatic increase of the spin-orbit coupling and will not change our findings regarding the requirement to fine-tune the wire radius. We conclude, therefore, that finding topological Majorana modes in full-shell nanowires will be quite challenging and will depend on considerable trial and error to achieve a lucky sweet spot in optimizing the spin-orbit coupling and chemical potential. The lack of a suitable tuning parameter in situ is a serious problem in this respect.

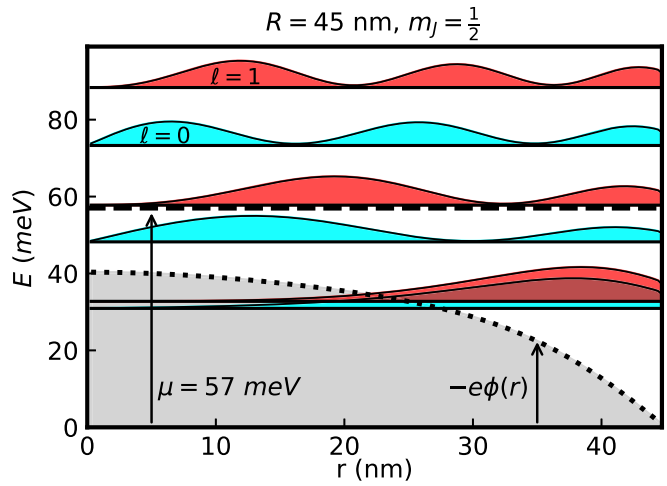

FIG. 4. Wave function profiles, $|\psi|^2$, of the first six $m_J = \frac{1}{2}$ states at $k_z = 0$ for a wire of radius $R = 45$ nm and $\mu = 57$ meV. The states are shifted vertically by their energies. The effective mean-field potential is also shown as a dotted line (gray filling), while the chemical potential is marked by the black dashed line. The $m_J = \frac{1}{2}$ states dominated by $\ell = 0$ and $\ell = 1$ components are shaded blue and red, respectively. Notice that the first two states are confined within the outer region $30 \leqslant r \leqslant 45$ nm where the radial electric field is maximum, while the other states are distributed over the entire cross section of the wire.

This work is supported by Microsoft Q, Laboratory for Physical Sciences, and NSF DMR-1414683.

[1] N. Read and D. Green, Phys. Rev. B **61**, 10267 (2000).
[2] A. Y. Kitaev, Phys. Usp. **44**, 131 (2001).
[3] C. Nayak, S. H. Simon, A. Stern, M. Freedman, and S. Das Sarma, Rev. Mod. Phys. **80**, 1083 (2008).
[4] S. Das Sarma, M. Freedman, and C. Nayak, npj Quantum Inf. **1**, 15001 (2015).
[5] J. D. Sau, R. M. Lutchyn, S. Tewari, and S. Das Sarma, Phys. Rev. Lett. **104**, 040502 (2010).
[6] R. M. Lutchyn, J. D. Sau, and S. Das Sarma, Phys. Rev. Lett. **105**, 077001 (2010).
[7] Y. Oreg, G. Refael, and F. von Oppen, Phys. Rev. Lett. **105**, 177002 (2010).
[8] V. Mourik, K. Zuo, S. M. Frolov, S. R. Plissard, E. P. A. M. Bakkers, and L. P. Kouwenhoven, Science **336**, 1003 (2012).
[9] M. T. Deng, C. L. Yu, G. Y. Huang, M. Larsson, P. Caroff, and H. Q. Xu, Nano Lett. **12**, 6414 (2012).
[10] A. Das, Y. Ronen, Y. Most, Y. Oreg, M. Heiblum, and H. Shtrikman, Nat. Phys. **8**, 887 (2012).
[11] H. O. H. Churchill, V. Fatemi, K. Grove-Rasmussen, M. T. Deng, P. Caroff, H. Q. Xu, and C. M. Marcus, Phys. Rev. B **87**, 241401(R) (2013).
[12] A. D. K. Finck, D. J. Van Harlingen, P. K. Mohseni, K. Jung, and X. Li, Phys. Rev. Lett. **110**, 126406 (2013).
[13] S. M. Albrecht, A. P. Higginbotham, M. Madsen, F. Kuemmeth, T. S. Jespersen, J. Nygård, P. Krogstrup, and C. M. Marcus, Nature (London) **531**, 206 (2016).
[14] M. T. Deng, S. Vaitiekenas, E. B. Hansen, J. Danon, M. Leijnse, K. Flensberg, J. Nygård, P. Krogstrup, and C. M. Marcus, Science **354**, 1557 (2016).
[15] F. Nichele, A. C. C. Drachmann, A. M. Whiticar, E. C. T. O'Farrell, H. J. Suominen, A. Fornieri, T. Wang, G. C. Gardner, C. Thomas, A. T. Hatke, P. Krogstrup, M. J. Manfra, K. Flensberg, and C. M. Marcus, Phys. Rev. Lett. **119**, 136803 (2017).
[16] H. Zhang, O. Gul, S. Conesa-Boj, M. P. Nowak, M. Wimmer, K. Zuo, V. Mourik, F. K. de Vries, J. van Veen, M. W. de Moor, J. D. Bommer, D. J. van Woerkom, D. Car, S. R. Plissard, E. P. Bakkers, M. Quintero-Perez, M. C. Cassidy, S. Koelling, S. Goswami, K. Watanabe, T. Taniguchi, and L. P. Kouwenhoven, Nat. Commun. **8**, 16025 (2017).
[17] O. Gül, H. Zhang, J. D. S. Bommer, M. W. A. de Moor, D. Car, S. R. Plissard, E. P. A. M. Bakkers, A. Geresdi, K. Watanabe, T. Taniguchi, and L. P. Kouwenhoven, Nat. Nanotechnol. **13**, 192 (2018).
[18] S. Das Sarma, J. D. Sau, and T. D. Stanescu, Phys. Rev. B **86**, 220506(R) (2012).
[19] G. Kells, D. Meidan, and P. W. Brouwer, Phys. Rev. B **86**, 100503(R) (2012).
[20] C. Moore, T. D. Stanescu, and S. Tewari, Phys. Rev. B **97**, 165302 (2018).
[21] C.-X. Liu, J. D. Sau, T. D. Stanescu, and S. Das Sarma, Phys. Rev. B **96**, 075161 (2017).
[22] A. Vuik, B. Nijholt, A. R. Akhmerov, and M. Wimmer, arXiv:1806.02801.
[23] C. Reeg, O. Dmytruk, D. Chevallier, D. Loss, and J. Klinovaja, Phys. Rev. B **98**, 245407 (2018).
[24] T. D. Stanescu and S. Tewari, arXiv:1811.02557.
[25] S. Vaitiekenas, M.-T. Deng, P. Krogstrup, and C. M. Marcus, arXiv:1809.05513.
[26] R. M. Lutchyn, G. W. Winkler, B. van Heck, T. Karzig, K. Flensberg, L. I. Glazman, and C. Nayak, arXiv:1809.05512.
[27] A. Vuik, D. Eeltink, A. R. Akhmerov, and M. Wimmer, New J. Phys. **18**, 033013 (2016).
[28] B. D. Woods, T. D. Stanescu, and S. Das Sarma, Phys. Rev. B **98**, 035428 (2018).
[29] A. E. G. Mikkelsen, P. Kotetes, P. Krogstrup, and K. Flensberg, Phys. Rev. X **8**, 031040 (2018).
[30] A. E. Antipov, A. Bargerbos, G. W. Winkler, B. Bauer, E. Rossi, and R. M. Lutchyn, Phys. Rev. X **8**, 031041 (2018).
[31] P. Wójcik, A. Bertoni, and G. Goldoni, Phys. Rev. B **97**, 165401 (2018).
[32] R. Winkler, *Spin-Orbit Coupling Effects in Two-Dimensional Electron and Hole Systems* (Springer, New York, 2003).
[33] W. Kohn and J. M. Luttinger, Phys. Rev. **98**, 915 (1955).
[34] J. M. Luttinger, Phys. Rev. **102**, 1030 (1956).
[35] Y.-C. Chang, Phys. Rev. B **37**, 8215 (1988).
[36] J. P. Loehr, Phys. Rev. B **50**, 5429 (1994).
[37] O. Marquardt, D. Mourad, S. Schulz, T. Hickel, G. Czycholl, and J. Neugebauer, Phys. Rev. B **78**, 235302 (2008).
[38] N. Luo, G. Liao, and H. Q. Xu, AIP Adv. **6**, 125109 (2016).
[39] See Supplemental Material at http://link.aps.org/supplemental/10.1103/PhysRevB.99.161118 for details regarding the $\vec{k}\cdot\vec{p}$ model, electrostatic calculation, spin-orbit coupling parameter extraction, and the results of fitting the effective mass as a function of chemical potential. References [40–44] are included in the Supplemental Material.
[40] E. O. Kane, J. Phys. Chem. Solids **1**, 249 (1957).
[41] I. Ivashev, Theoretical investigations of zinc blende and wurtzite semiconductor quantum wells on the rotated substrates, Master's thesis, Wilfrid Laurier University, Canada, 2016.
[42] V. Arsoski, N. Čukarić, M. Tadić, and F. Peeters, Comput. Phys. Commun. **197**, 17 (2015).
[43] G. W. Winkler, D. Varjas, R. Skolasinski, A. A. Soluyanov, M. Troyer, and M. Wimmer, Phys. Rev. Lett. **119**, 037701 (2017).
[44] V. Laliena and J. Campo, J. Phys. A: Math. Theor. **51**, 325203 (2018).
[45] W. S. Cole, S. Das Sarma, and T. D. Stanescu, Phys. Rev. B **92**, 174511 (2015).
[46] T. D. Stanescu and S. Das Sarma, Phys. Rev. B **96**, 014510 (2017).
[47] C. Reeg, D. Loss, and J. Klinovaja, Phys. Rev. B **97**, 165425 (2018).
[48] P. E. Faria Junior, T. Campos, C. M. O. Bastos, M. Gmitra, J. Fabian, and G. M. Sipahi, Phys. Rev. B **93**, 235204 (2016).
[49] T. Campos, P. E. Faria Junior, M. Gmitra, G. M. Sipahi, and J. Fabian, Phys. Rev. B **97**, 245402 (2018).